INTERNATIONAL JOURNAL FOR NUMERICAL METHODS IN FLUIDS, VOL. 23, 271–293 (1996)

A CELL VERTEX ALGORITHM FOR THE INCOMPRESSIBLE NAVIER–STOKES EQUATIONS ON NON-ORTHOGONAL GRIDS

J. P. JESSEE AND W. A. FIVELAND

Research and Development Division, Babcock & Wilcox, 1562 Beeson Street, Alliance, OH, U.S.A.

SUMMARY

The steady, incompressible Navier–Stokes (N–S) equations are discretized using a cell vertex, finite volume method. Quadrilateral and hexahedral meshes are used to represent two- and three-dimensional geometries respectively. The dependent variables include the Cartesian components of velocity and pressure. Advective fluxes are calculated using bounded, high-resolution schemes with a deferred correction procedure to maintain a compact stencil. This treatment insures bounded, non-oscillatory solutions while maintaining low numerical diffusion. The mass and momentum equations are solved with the projection method on a non-staggered grid. The coupling of the pressure and velocity fields is achieved using the Rhie and Chow interpolation scheme modified to provide solutions independent of time steps or relaxation factors. An algebraic multigrid solver is used for the solution of the implicit, linearized equations.

A number of test cases are anlaysed and presented. The standard benchmark cases include a lid-driven cavity, flow through a gradual expansion and laminar flow in a three-dimensional curved duct. Predictions are compared with data, results of other workers and with predictions from a structured, cell-centred, control volume algorithm whenever applicable. Sensitivity of results to the advection differencing scheme is investigated by applying a number of higher-order flux limiters: the MINMOD, MUSCL, OSHER, CLAM and SMART schemes. As expected, studies indicate that higher-order schemes largely mitigate the diffusion effects of first-order schemes but also shown no clear preference among the higher-order schemes themselves with respect to accuracy. The effect of the deferred correction procedure on global convergence is discussed.

KEY WORDS: finite volume; cell vertex; pressure–velocity coupling; high-resolution schemes; non-orthogonal

1. INTRODUCTION

Motivation and objective

Many practical CFD problems involve incompressible flow in complex, three-dimensional geometries. Examples include serpentine ducts, curved turbomachinery parts and curved internals in fossil fuel burners. The need to model flows in these geometries has motivated the development of computational algorithms for non-orthogonal and unstructured grids. Over the last decade, much progress has been made in reaching that goal. The present work attempts to implement and extend some of the more promising features of a number of previous works with the objective of developing accurate, efficient and robust algorithms for the solution of the N–S equations for general two- and three-dimensional, unstructured and non-orthogonal meshes.

Background

To facilitate a systematic review, the current topic will be divided into a number of constituent parts: (i) spatial discretization method (finite volume, finite element, etc.), (ii) advection differencing scheme, (iii) pressure–velocity coupling method and (iv) overall solution algorithm.

CCC 0271–2091/96/030271–23
© 1996 by John Wiley & Sons, Ltd.

Received 14 April 1995
Revised 12 October 1995

Spatial discretization methods. Finite volume (FV) and finite element (FE) methods have been the most widely applied methods. FV methods have the advantage that they are strictly conservative and are somewhat more intuitively based than FE methods. In recent years, however, some aspects of the formulations have become indistinguishable. Barth[1] has shown the equivalence of the Galerkin FE and cell vertex FV formulations of the Laplacian and Hessian operators on linear triangular and tetrahedral cells. Similarly, total variational diminishing (TVD) schemes for advection terms are now being equally applied to both FE and FV formulations.

For FV formulations, two basic grid arrangements have been used: cell-centred and cell vertex arrangements. Cell-centred arrangements have been predominantly applied to curvilinear and general co-ordinate formulations, both orthogonal and non-orthogonal. While such formulations permit meshes which conform to curved boundaries, they are typically restricted to structured or block-structured grids, which limit coarse-to-fine grid transitions. In contrast, both cell-centred[2] and cell vertex[3] arrangements have been applied to unstructured, non-orthogonal meshes using Cartesian components of velocity or momentum as dependent variables. These formulations not only support grids which conform to complex boundaries, but also permit grid transitions needed to accurately capture steep solution gradients. Although cell vertex arrangements are typically used for unstructured meshes, cell-centred arrangements are equally valid and neither arrangement presently shows clear superiority over the other.

Advection differencing schemes. Regardless of the general discretization procedures, special treatment of the advective flux is required to simultaneously provide accuracy, boundedness and stability. Lower-order methods such as the upwind or hybrid schemes are bounded and stable but are also highly diffusive. In contrast, early higher-order schemes such as QUICK[4] are more accurate but lack boundedness. Many remedies have been proposed. A common approach involves flux blending, in which an antidiffusive flux is added to a stable first-order scheme or a diffusive flux is added to an accurate but unbounded higher-order scheme. Although often effective, flux-blending schemes tend to be computationally complex and expensive and/or they often fail to provide the balance between accuracy and boundedness.[5] An alternative and more attractive approach is the family of high-resolution (HR) flux limiters. These schemes are based on composite flux expressions which insure boundedness in regions of sharp gradients and also provide high resolution in monotonic regions. The total variational diminishing (TVD) schemes of the compressible flow community are examples of this type of scheme.

Pressure–velocity coupling. The primitive variable solution of the incompressible N–S equations is complicated by the relationship of the dependent variables. The momentum equations contain gradients of pressure which are not expressible in terms of the velocity components, and the pressure is indirectly linked to the continuity equation through the velocity field. The collocation of pressures and velocities with the use of central differencing leads to a decoupling of the velocity and pressure fields which may introduce oscillations in the pressure solution (i.e. checkerboard pressure field). Early remedies to the problem employed staggered grid arrangements.[6] The increased complication of implementing a staggered grid arrangement on non-orthogonal and unstructured meshes motivated the development of pressure–velocity coupling methods for non-staggered or collocated grids. Popular methods include Rhie and Chow interpolation[7] and artificial dissipation schemes.[8,9] In artificial dissipation schemes, second- and/or fourth-order smoothing terms are added to the momentum equations; however, these terms often corrupt the accuracy of the overall scheme and a debate still remains on the best approach to construct the dissipation operators. The Rhie and Chow method involves a special interpolation procedure for cell face velocities. The success of the method may be attributed to the fact that the staggering idea is implicitly adopted.[10] Rhie and Chow interpolation with a modification by

Majumdar[11] has exhibited the same accuracy and convergence characteristics as the staggered grid arrangement.[12–14]

Solution algorithms. Typical methods for solving the coupled equations include projection, pseudocompressibility and coupled methods. For practical problems, fully coupled approaches are hampered by large storage and computational requirements, although block implicit methods[15] mitigate this problem somewhat but at a the cost of reduced spatial coupling. Pseudocompressibility methods have gained some popularity because they are natural extensions of explicit compressible time-stepping schemes which do not require the implicit solution of a pressure Poisson equation of projection methods. However, the reliability and convergence characteristics of these methods are largely dependent on the chosen value of the compressibility factor.[16] Also, the advent of algebraic multigrid solution algorithms has simplified the implicit solution of the pressure Poisson equation.

Current approach

In the current algorithm the incompressible Navier–Stokes (N–S) equations are spatially discretized using a cell vertex finite volume method. Advective fluxes are calculated with bounded, high-resolution differencing schemes. The coupling of the pressure and velocity fields on the non-staggered grid is achieved using the Rhie and Chow interpolation scheme[7] with an extension due to Majumdar[11] to provide solutions independent of relaxation factors or time steps. The mass and momentum equations are solved with a single-step projection method. An algebraic multigrid solver is used for the solution of the implicit, linearized equations. Flux calculations are performed using a cell edge data structure to facilitate vectorization.

Section 2 outlines the mathematical formulation in which the governing Navier–Stokes equations, the discretization procedure and the flow algorithm are presented. Section 3 presents computational results for three examples. Finally, Section 4 summarizes the work, states conclusions based on the example cases and recommends future directions.

2. MATHEMATICAL FORMULATIONS

2.1. Governing equations

For ease of presentation the solution procedure is outlined for two-dimensional space. The transient, incompressible, conservation equations for mass, momentum and a scalar quantity are given as

$$\int_V \frac{\partial Q}{\partial t}\,\mathrm{d}V + \oint_S (F^{\mathrm{I}}, G^{\mathrm{I}})\cdot\hat{n}\,\mathrm{d}S + \oint_S (F^{\mathrm{V}}, G^{\mathrm{V}})\cdot\hat{n}\,\mathrm{d}S - \int_V S\,\mathrm{d}V = 0, \tag{1}$$

where Q is the dependent variable vector,

$$Q = \rho\Phi = \rho\begin{Bmatrix} 1 \\ U \\ V \\ \phi \end{Bmatrix}, \tag{2a}$$

F^{I} and G^{I} are elements of the row matrix of the inviscid fluxes,

$$F^{\mathrm{I}} = \left\{ \begin{matrix} \rho U \\ \rho U^2 + p \\ \rho UV \\ \rho U\phi \end{matrix} \right\}, \qquad G^{\mathrm{I}} = \left\{ \begin{matrix} \rho V \\ \rho UV \\ \rho V^2 + p \\ \rho V\phi \end{matrix} \right\}, \tag{2b}$$

F^{V} and G^{V} are elements of the row matrix of the viscous fluxes,

$$F^{\mathrm{V}} = \left\{ \begin{matrix} 0 \\ -\tau_{xx} \\ -\tau_{xy} \\ -\Gamma_\phi \dfrac{\partial \phi}{\partial x} \end{matrix} \right\}, \qquad G^{\mathrm{V}} = \left\{ \begin{matrix} 0 \\ -\tau_{yx} \\ -\tau_{yy} \\ -\Gamma_\phi \dfrac{\partial \phi}{\partial y} \end{matrix} \right\}, \tag{2c}$$

and S is the volumetric source vector. U and V are the Cartesian velocity components in the x- and y-direction respectively, p is the static pressure, ϕ is a scalar quantity, ρ is the gas density, Γ is the molecular diffusivity and τ is a stress tensor. The transient terms have been included as a means of applying relaxation in pursuit of a steady state solution. Time-accurate solutions are not of prime importance.

2.2. *Geometrical basis*

In the cell vertex form of the finite volume method (FVM) the nodes of the control volumes are located at the vertices of the elements. This type of discretization is similar to the control-volume-based finite element method[17,18] and the subdomain weighted residual method[19] in the finite element community.

The grid is formed by dividing the spatial domain into a number of non-overlapping elements as shown in Figure 1. In the present work, quadrilateral (four-node) and hexahedral (eight-node) isoparameteric elements from the Lagrange family are used to represent two- and three-dimensional domains respectively. The discretization methods may easily be extended to other types of elements, including linear triangular elements for 2D domains[1,17,20] and tetrahedral elements for 3D domains.[3] The quadrilateral and hexahedral elements and the associated shape functions are defined by Zienkiewicz and Taylor.[21] A typical quadrilateral element is shown in Figure 2 with the local co-ordinate system (ξ_1, ξ_2). For the isoparametric basis the origin of the local co-ordinate system is defined as the average of the element vertex co-ordinates.

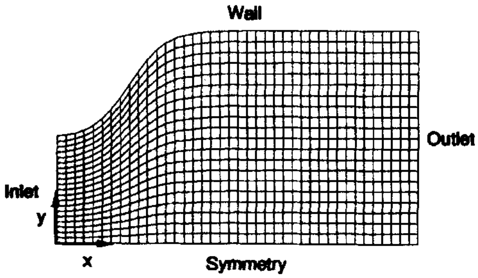

Figure 1. Sample computational mesh

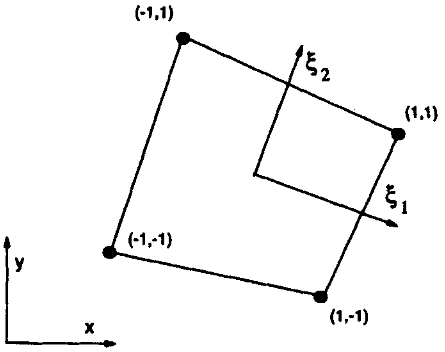

Figure 2. Parametric co-ordinate system on a sample quadrilateral element

As shown in Figure 3, nodes are located at the corners or vertices of the elements and a control volume is associated with each node. All dependent variables (pressure, velocities, etc.) are calculated and stored at the nodal locations. The control volume boundaries are created by dividing elements along the lines $\xi_1 = 0$ and $\xi_2 = 0$. This is known as a dual-median mesh.[22] As noted by Schneider,[23] this choice guarantees the alignment of control volume edges. The boundary of a given control volume is defined by a set of discrete surfaces. Each surface forms a boundary between two adjacent control volumes and is composed of a number of subsurfaces: two in 2D and four in 3D. The area of each surface is the sum of the subsurface areas and the surface unit normal is the area-weighted average of the unit normal vectors of the subsurfaces. The integration point for each surface is taken at the midpoint along the element edge connecting two adjacent nodes (see Figure 3).

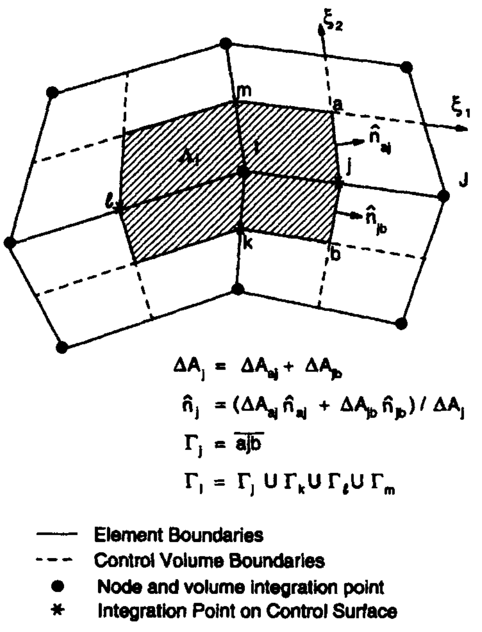

$$\Delta A_j = \Delta A_{aj} + \Delta A_{jb}$$

$$\hat{n}_j = (\Delta A_{aj}\,\hat{n}_{aj} + \Delta A_{jb}\,\hat{n}_{jb}) / \Delta A_j$$

$$\Gamma_j = \overline{ajb}$$

$$\Gamma_I = \Gamma_j \cup \Gamma_k \cup \Gamma_\ell \cup \Gamma_m$$

Figure 3. Dual-median mesh schematic

2.3. Discretization of governing equations

General conservation equation

The spatial domain is divided into a number of control volumes as defined in the previous subsection. For each control volume the governing equations are written in integral form as

$$\int_{\Lambda_I} \frac{\partial}{\partial t}(\rho\phi)\,\mathrm{d}\Lambda + \oint_{\Gamma_I} (\rho\vec{u}\phi - \Gamma\nabla\phi)\cdot\hat{n}\,\mathrm{d}\Gamma - \int_{\Lambda_I} S^{\phi}\,\mathrm{d}\Lambda = 0, \tag{3}$$

where $\hat{n}$ is the outward unit normal and Λ_I and Γ_I denote the domain and boundary of control volume I respectively. Equation (3) essentially states that the rate of change within the control volume balances the net transport rate across the volume boundaries and production rate within the volume. In the discretization procedure the boundary integral is represented by the sum of integrals over the control surfaces bounding the volume. The portion of boundary represented by the control surface is denoted by Γ_j. Integrals over control volumes and control surfaces are evaluated using single-point quadratures. To simplify the procedure, the terms in equation (3) will be discretized individually.

Transient term. The transient term is represented by a first-order backward difference in time (implicit Euler scheme) and a lumped mass approximation in space:

$$\int_{\Lambda_I} \frac{\partial(\rho\phi)}{\partial t}\,\mathrm{d}\Lambda = \rho\Delta V_I \frac{\phi_I - \phi_I^0}{\Delta t}, \tag{4}$$

where ΔV_I is the volume of the control volume, Δt is the time step and the subscript I on the other terms denotes the node or control volume. The contribution to the global system of discrete equations may be written as

$$\int_{\Lambda_I} \frac{\partial(\rho\phi)}{\partial t}\,\mathrm{d}\Lambda = a_{II}^{\phi,\mathrm{t}}\phi_I - b_I^{\phi,\mathrm{t}}. \tag{5}$$

The first term on the RHS represents any implicit dependence of the transient term on the dependent variable and the second term represents the explicit portion. The superscripts on the coefficient a denote the conservation equation and the respective term (e.g. 't' denotes the transient portion). The subscripts denote the index of the control volume and the nodal subscript of the multiplying dependent variable respectively. The subscripts and superscripts on b follow the same convention. The first-order temporal approximation is considered principally because transient solutions are not of primary importance with regard to the present work. With some additional complexity in the flow solution algorithm and application of boundary conditions, second-order temporal accuracy may be obtained by using alternative time discretization schemes.

Advection term. The advection portion of equation (3) is approximated for a control surface j as

$$\int_{\Gamma_j} (\rho\vec{u}\phi)\cdot\hat{n}\,\mathrm{d}\Gamma = C_j\phi_j, \tag{6a}$$

where

$$C_j = \Delta A_j \rho_j \vec{u}_j \cdot \hat{n}_j \tag{6b}$$

and again ΔA_j is the area of the jth control surface and the integrand is evaluated at the integration point. Owing to the physical nature of the advection, the evaluation of the RHS of equation (6a) requires special consideration. As outlined in Section 1, workers have employed a wide variety of techniques.

Recently the family of high-resolution (HR) flux limiters has received considerable attention owing to a number of desirable features: the schemes are bounded, highly accurate (low numerical diffusion) and fairly easy to implement. The advective flux at faces of control volumes is calculated using composite flux limiters which enforce monotonicity. Darwish[5] and Darwish and Moukalled[24] review a number of these schemes in terms of the normalized variable formulation.

In this work a number of HR schemes are extended for unstructured, non-orthogonal grids following the approach of Lyra *et al.*[25] and Cabello and Morgan[26] for 2D, unstructured triangular meshes. To facilitate the presentation, a 2D mesh of quadrilateral elements is considered, but the formulation is equally valid in three dimensions. As before, control volumes are formed for each element vertex. Integration points are located at the midpoints of the element edges as shown in Figure 4 and thus lie directly between two nodes. A three-point stencil is formed by introducing a dummy node upstream of the integration point as shown by point U in Figure 4. Cabello and Morgan[26] placed point U such that points U, C and D are located equidistantly along a line formed by the edge. However, for a rapid change in cell size this procedure may place the dummy node several cells away from the integration point or outside the domain. For this reason, point U was located at a position where the line CD intersects the face of the upstream element. The advective flux is then determined using the three-point stencil (UCD) and the normalized variable formulation (NVF)[27] with a modification for non-uniform grids.[24]

Five bounded, high-resolution schemes were considered: Roe's MINMOD scheme,[28] OSHER,[29] Van Leer's MUSCL[30] and CLAM[31] schemes and Gaskell and Lau's SMART scheme.[32] As noted by Darwish,[5] the MINMOD scheme is similar to the SOUCOUP scheme of Zhu and Rodi.[33] For conciseness, only the MINMOD and CLAM schemes are presented here. Descriptions of the other schemes may be found in the original references or in Reference 24.

MINMOD or SOUCOUP

$$\tilde{\phi}_{\mathrm{f}} = \frac{\tilde{x}_{\mathrm{f}}}{\tilde{x}_{\mathrm{C}}}\tilde{\phi}_{\mathrm{C}}, \quad 0<\tilde{\phi}_{\mathrm{C}}<\tilde{x}_{\mathrm{C}}, \tag{7a}$$

$$\tilde{\phi}_{\mathrm{f}} = \frac{\tilde{x}_{\mathrm{C}}-\tilde{x}_{\mathrm{f}}}{\tilde{x}_{\mathrm{C}}-1} + \frac{\tilde{x}_{\mathrm{f}}-1}{\tilde{x}_{\mathrm{C}}-1}\tilde{\phi}_{\mathrm{C}}, \quad \tilde{x}_{\mathrm{C}}<\tilde{\phi}_{\mathrm{C}}<1, \tag{7b}$$

$$\tilde{\phi}_{\mathrm{f}} = \tilde{\phi}_{\mathrm{C}}, \quad \text{elsewhere.} \tag{7c}$$

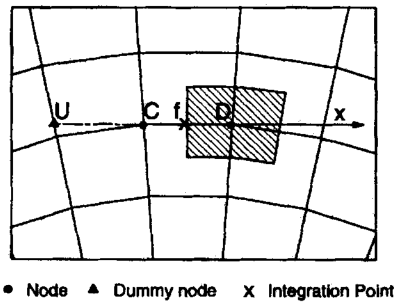

Figure 4. Location of upstream dummy node

CLAM

$$\tilde{\phi}_{\mathrm{f}} = \frac{\tilde{x}_{\mathrm{C}}^2 - \tilde{x}_{\mathrm{f}}}{\tilde{x}_{\mathrm{C}}(\tilde{x}_{\mathrm{C}} - 1)}\tilde{\phi}_{\mathrm{C}} + \frac{\tilde{x}_{\mathrm{f}} - \tilde{x}_{\mathrm{C}}}{\tilde{x}_{\mathrm{C}}(\tilde{x}_{\mathrm{C}} - 1)}\tilde{\phi}_{\mathrm{C}}^2, \quad 0 < \tilde{\phi}_{\mathrm{C}} < 1, \tag{8a}$$

$$\tilde{\phi}_{\mathrm{f}} = \tilde{\phi}_{\mathrm{C}}, \quad \text{elsewhere.} \tag{8b}$$

The normalized variables, denoted with tildes, are defined as

$$\tilde{\phi} = \frac{\phi - \phi_{\mathrm{U}}}{\phi_{\mathrm{D}} - \phi_{\mathrm{U}}}, \qquad \tilde{x} = \frac{x - x_{\mathrm{U}}}{x_{\mathrm{D}} - x_{\mathrm{U}}}. \tag{9}$$

The value of the dependent variable for the flux expression is obtained from the normalized face value and equation (9):

$$\phi_{\mathrm{f}} = \frac{\phi_{\mathrm{D}} - \phi_{\mathrm{U}}}{\phi_{\mathrm{U}}}\tilde{\phi}_{\mathrm{f}}. \tag{10}$$

The flux term is applied using a deferred correction technique to reduce the stencil of the discrete equations. In this technique the advective flux is written as the sum of a first-order upwind term and a second term which provides higher accuracy. The first-order upwind term is treated implicitly, while the correction term is treated explicitly and placed in the source term. The procedure guarantees that the discrete system of equations is diagonally dominant—a very important feature for iterative solvers. In addition, the compact implicit stencil reduces both the storage requirements for coefficients and the computational requirements for the solution of the equations. These advantages are gained at the expense of making the equations more explicit, which may necessitate more global iterations or time steps.

Returning to the control volume in Figure 3, a contravariant velocity is assumed between nodes I and J such that nodes J and I correspond to nodes C and D respectively. The expression for the dependent variable at the face or control surface, ϕ_{f}, may be substituted into equation (6a) to form the advection contribution for control surface j:

$$\int_{\Gamma_j} (\rho\vec{u}\phi)\cdot\hat{n}\,\mathrm{d}\Gamma = C_j\phi_{\mathrm{f}} = C_j\phi_J + C_j(\phi_{\mathrm{f}} - \phi_J). \tag{11}$$

By treating the last term in equation (11) explicitly, the equation may be recast as

$$\int_{\Gamma_j} (\rho\vec{u}\phi)\cdot\hat{n}\,\mathrm{d}\Gamma = a_{IJ}^{\phi,\mathrm{a}}\phi_J - b_I^{\phi,\mathrm{a}}. \tag{12}$$

A similar expression may be written for a velocity in the opposite direction.

Diffusion term. The diffusion portion of equation (3) is approximated for a typical control surface j as

$$\int_{\Gamma_j} -\Gamma\,\nabla\phi\cdot\hat{n}\,\mathrm{d}\Gamma = -(\Gamma\,\Delta A\,\nabla\phi\cdot\hat{n})_j, \tag{13}$$

where ΔA_j is the area of the control surface and all other quantities on the RHS are evaluated at the surface integration point. The gradient at the surface integration point is expressed in terms of the elemental basis functions and the nodal values of the dependent variable. By substituting this gradient expression and simplifying, equation (13) may be written as

$$\int_{\Gamma_j} -\Gamma\, \nabla\phi \cdot \hat{n}\, \mathrm{d}\Gamma = a_{IJ}^{\phi,\mathrm{d}}(\phi_I - \phi_J) - b_I^{\phi,\mathrm{d}}, \tag{14}$$

where the first and second terms on the right-hand side represent the orthogonal and non-orthogonal portions of the diffusion term respectively. The superscript 'd' denotes the diffusion contribution to the global system of equations and the other subscripts and superscripts are defined as before. The non-orthogonal term is treated explicitly to reduce storage and computational requirements.

Source term. The last integral in equation (3) is approximated for a typical control volume as

$$\int_{\Lambda_I} S^{\phi}\, \mathrm{d}\Lambda = \Delta V_I S^{\phi}|_I. \tag{15}$$

The evaluation of the source S^{ϕ} is made at the node of the control volume (i.e. lumped mass approximation). The contribution to the global system of equations is

$$\int_{\Lambda_I} S^{\phi}\, \mathrm{d}\Lambda = -a_{II}^{\phi,\mathrm{s}}\phi_I + b_I^{\phi,\mathrm{s}}, \tag{16}$$

where the first and second terms on the RHS represent the implicit and explicit portions of the source term respectively.

Assembled equations. The previous subsections have defined the discrete representations to the various terms in the control volume integral equation. By considering all contributions, the discrete conservation equations may be expressed as

$$(a_{II}^{\phi,\mathrm{t}} + a_{II}^{\phi})\phi_I + \sum_{\substack{J \\ J\neq I}} a_{IJ}^{\phi}\phi_J = b_I^{\phi} + a_{II}^{\phi,\mathrm{t}}\phi_I^0, \tag{17}$$

where

$$a_{II}^{\phi} = a_{II}^{\phi,\mathrm{d}} + a_{II}^{\phi,\mathrm{a}} + a_{II}^{\phi,\mathrm{s}}, \tag{18a}$$

$$a_{IJ}^{\phi} = a_{IJ}^{\phi,\mathrm{d}} + a_{IJ}^{\phi,\mathrm{a}}, \tag{18b}$$

$$b_I^{\phi} = b_I^{\phi,\mathrm{d}} + b_I^{\phi,\mathrm{a}} + b_I^{\phi,\mathrm{s}}. \tag{18c}$$

The summation extends over global nodes with non-zero coefficients.

Momentum conservation equations

The momentum conservation equations are discretized using the procedures of the previous subsection. The vector control volume equation is

$$\int_{\Lambda_I} \frac{\partial}{\partial t}(\rho\vec{u})\, \mathrm{d}\Lambda + \oint_{\Gamma_I} (\rho\vec{u} \otimes \vec{u} - \tau) \cdot \hat{n}\, \mathrm{d}\Gamma + \oint_{\Gamma_I} p\hat{n}\, \mathrm{d}\Gamma - \int_{\Lambda_I} \vec{S}^{u}\, \mathrm{d}\Lambda = 0. \tag{19}$$

Each component of the above equation represents a respective component of the vector momentum equation. The component momentum equations are in the form of equation (3) and the terms have previously been discretized, with the exception of the pressure term which is approximated using the surface quadrature

$$\int_{\Gamma_j} p\hat{n}\,\mathrm{d}\Gamma = \Delta A_j p_j \hat{n}_j. \tag{20}$$

The pressure at the integration point on control surface j is evaluated using the nodal pressures and basis functions. In the present work a segregated solution method is used and thus the pressure gradients are treated explicitly with respect to the momentum equations:

$$\int_{\Gamma_j} p\hat{n}\,\mathrm{d}\Gamma = -(b_I^{U,p}\hat{i} + b_I^{V,p}\hat{j}). \tag{21}$$

The discrete momentum equations may be expressed as

$$(a_{II}^{U,\mathrm{t}} + a_{II}^{U})U_I + \sum_{\substack{J \\ J\neq 1}} a_{IJ}^{U} U_J = b_I^{U} + b_I^{U,p} + a_{II}^{U,\mathrm{t}} U_I^0, \tag{22a}$$

$$(a_{II}^{V,\mathrm{t}} + a_{II}^{V})V_I + \sum_{\substack{J \\ J\neq 1}} a_{IJ}^{V} V_J = b_I^{V} + b_I^{V,p} + a_{II}^{V,\mathrm{t}} V_I^0, \tag{22b}$$

where the coefficients and constants follow the previously defined convention.

Mass conservation equation

A control volume equation for the conservation of mass may be written as

$$\int_{\Lambda_I} \frac{\partial\rho}{\partial t}\,\mathrm{d}\Lambda + \oint_{\Gamma_I} \rho\vec{u}\cdot\hat{n}\,\mathrm{d}\Gamma = 0. \tag{23}$$

If a temporally invariant density is assumed, the first term may be neglected. For a typical control surface the second integral approximated as

$$\int_{\Gamma_j} \rho\vec{u}\cdot\hat{n}\,\mathrm{d}\Gamma = \rho_j\,\Delta A_j(un_x + vn_y)_j, \tag{24}$$

where the subscript j denotes the jth surface. By considering all surfaces of a control volume, the discrete continuity equation may be expressed as

$$\sum_j a_{Ij}^{cu} u_j + \sum_j a_{Ij}^{cv} j = 0, \tag{25}$$

where the summation extends over all surface integration points on the boundary of the control volume and the superscript 'c' denotes the continuity equation. The above representation involves velocities at the integration points in contrast to values at the nodes.

The coupled mass and momentum equations are solved with a projection method. The following subsections detail the interpolation scheme needed to close the system of discrete equations and the overall flow algorithm respectively.

2.4. *Pressure–velocity coupling*

The discrete equations (22a), (22b) and (25) are not in closed form because they contain more unknowns than equations; they contain velocities at both the control volume faces and control volume centres. To close the equations, the face values must be expressed in terms of the nodal values.

The face velocities are calculated using a form of Rhie and Chow interpolation.[7,11,12] This method effectively couples the pressure and velocity fields and eliminates checkerboard pressure solutions. The unstructured grid formulation follows the work of Prakash and Patankar.[20]

After some rearrangement the discrete momentum equations (22a) and (22b) may be written in the form

$$\vec{u}_I = \vec{H}_I + D_I \langle \nabla p \rangle_I + \beta_I \vec{u}^{\,0}_I, \tag{26}$$

where

$$\vec{H}_I = \frac{1}{\gamma_I}\left(-\sum_{\substack{J\\ J\neq I}} a^U_{IJ} U_J + b^U_I\right)\hat{i} + \frac{1}{\gamma_I}\left(-\sum_{\substack{J\\ J\neq I}} a^V_{IJ} V_J + b^V_I\right)\hat{j}, \tag{27a}$$

$$D_I = -\frac{\Delta V_I}{\gamma_I}, \tag{27b}$$

$$\beta_I = \frac{1}{\gamma_I}\left(\frac{\rho \Delta V}{\Delta t}\right)_I, \qquad \gamma_I = \left(\frac{\rho \Delta V}{\Delta t}\right)_I - \sum_{\substack{J\\ J\neq I}} a_{IJ}, \tag{27c}$$

$$\langle \nabla p \rangle_I = \frac{1}{\Delta V_I}(-b_I^{U,p})\hat{i} + \frac{1}{\Delta V_I}(-b_I^{V,p})\hat{j}. \tag{27d}$$

The superscript 0 denotes values from the previous time step or iterate. The sum of the neighbour coefficients in the γ-term only include contributions from advection and diffusion, which are the same for all components of the vector momentum equation. This sum is a positive quantity, since the implicit neighbour coefficients are negative (note the sign convection for coefficients). The implicit portions of the sources are grouped into the H-term.

By following the approach of Prakash and Patankar[20] and an extension of Majumdar,[11] the velocities at the surface integration points are expressed as

$$\vec{u}_i = \vec{H}_i + D_i \, \nabla p_i + \beta_i \vec{u}^{\,0}_i. \tag{28}$$

The integration point values $\vec{H}_i$, D_i, and β_i are obtained from linear interpolation of the nodal values, while the pressure gradients are calculated using the nodal pressures and the local gradients of the basis functions. Equation (28) closes the discrete continuity and momentum equations.

2.5. *Flow solution algorithm*

The discretized mass and momentum equations are solved in a segregated approach using a standard projection method, the SIMPLE algorithm.[34] Other schemes may equally be used, including the pseudocompressibility method,[35] combinations of projection and pseudocompressibility techniques[16] and fully coupled methods. The projection method was selected because it conserves mass at each time step or iteration and requires substantially less storage than coupled, implicit algorithms.

The pressure correction equation is derived following a procedure of Hirsch[36] and Watterson.[3] The semidiscrete form of the vector momentum equation is considered:

$$\frac{\rho(\vec{u}^* - \vec{u}^n)}{\Delta t} = -\nabla \cdot (\rho \vec{u} \otimes \vec{u})^n - \nabla p^n + \nabla \cdot \tau^n, \tag{29}$$

where n denotes conditions at the beginning of the time step and the asterisk refers to intermediate values. The value $\vec{u}^*$ represents the intermediate velocity field after the solution of the momentum equations, which generally will not satisfy continuity. Corrections to the velocity and pressure fields,

$$\vec{u}^{n+1} = \vec{u}^* + \vec{u}', \tag{30}$$

$$p^{n+1} = p^n + p', \tag{31}$$

are sought such that the final values at $n+1$ satisfy both the continuity and momentum equations:

$$\nabla \cdot \rho \vec{u}^{n+1} = 0, \tag{32}$$

$$\frac{\rho(\vec{u}^{n+1} - \vec{u}^n)}{\Delta t} = -\nabla \cdot (\rho \vec{u} \otimes \vec{u})^n - \nabla p^{n+1} + \nabla \cdot \tau^n. \tag{33}$$

The relationship between the velocity and pressure corrections is obtained by subtracting equation (29) from (33):

$$\rho(\vec{u}^{n+1} - \vec{u}^*) = \rho \vec{u}' = -\Delta t \, \nabla p'. \tag{34}$$

The pressure correction equation may be derived by taking the divergence of the above equation and substituting equation (32):

$$-\nabla \cdot (\Delta t \nabla p') = -\nabla \cdot \rho \vec{u}^*. \tag{35}$$

The RHS is simply the defect in the continuity equation due to the intermediate velocity field. The pressure corrections provided by this equation may be used to correct the pressures and velocities using equations (31) and (34) respectively. The resulting pressure and velocity fields will satisfy the mass and momentum equations (32) and (33).

The spatially discrete form of the pressure correction equation is obtained using the finite volume method. The integral form of the pressure correction equation is

$$\int_{\Gamma_I} \Delta t \, \nabla p' \cdot \hat{n} \, d\Gamma = \int_{\Gamma_I} \rho \vec{u}^* \cdot \hat{n} \, d\Gamma. \tag{36}$$

This equation may be written in discrete form as

$$\sum_J a^{p'}_{IJ} \, p'_J = b^{p'}_I, \tag{37}$$

where the coefficients are calculated using the basis functions, the local time step and geometric considerations. The RHS is the discrete mass defect:

$$b^{p'}_I = \sum_j \Delta A_j (\rho \vec{u}^* \cdot \hat{n})_j. \tag{38}$$

The summation extends over all surface integration points on the boundary of the control volume.

The velocities at the control surfaces and nodes are corrected using discrete forms of equation (34):

$$\vec{u}_j^{n+1} = \vec{u}_j^{*} - \left(\frac{\Delta t}{\rho}\nabla p'\right)_j, \tag{39}$$

$$\vec{u}_I^{n+1} = \vec{u}_I^{*} - \left(\frac{\Delta t}{\rho}Gp'\right)_I, \tag{40}$$

where G represents the discrete gradient operator. The nodal pressures are updated using equation (31):

$$p_I^{n+1} = p_I^n + \alpha_p p_I', \tag{41}$$

where α_p represents pressure relaxation.

The solution algorithm is summarized as follows.

1. Initialize the pressure and velocity fields p^n and $\vec{u}^n$ (assume uniform pressure).
2. Solve the momentum equations for the nodal velocities $\vec{u}^*$.
3. Interpolate the nodal velocities to the faces using Rhie and Chow interpolation.
4. Solve the pressure correction equation for p'.
5. Calculate p^{n+1} by adding p' to p^n.
6. Calculate the velocities at the nodes and faces from the velocity correction equations.
7. Solve any scalar transport equations.
8. Take the corrected pressure field p^{n+1} as the assumed field p^n and repeat the procedure until convergence is obtained (e.g. return to step 2).

The above procedure is a single-stage time step scheme; however, the scheme may be extended to multiple stages as shown by Watterson.[3]

Steady state solutions were of prime importance with regard to the current work and a spatially varying time step was applied to speed convergence:

$$\Delta t_I = E\frac{\rho_I \Delta V_I}{-\sum\limits_{\substack{J \\ J\neq I}} a_{IJ}}, \tag{42}$$

where E represents the E-factor of Van Doormaal and Raithby.[37] The E-factor is analogous to the CFL number for high cell Peclet numbers and is related to the standard relaxation parameter by

$$E = \frac{\alpha}{1-\alpha}. \tag{43}$$

The discrete momentum and pressure correction equations form systems of linear, algebraic equations. These systems are solved individually with an algebraic multigrid solver which is based on the work of Hutchinson and Raithby[38] and Ruge and Stüben.[39] The non-orthogonal terms in the discrete pressure correction equation are treated semi-implicitly—they are updated on the finest level of the multigrid algorithm. This procedure is required to provide convergence on highly non-orthogonal grids. The above algorithm is equally applicable to three-dimensional geometries.

3. RESULTS

A number of standard benchmark cases were investigated to study the accuracy of the present algorithm, to test the sensitivity of the predictions to the differencing schemes and to determine the effect of the differencing scheme and deferred correction procedure on global convergence. The cases include a lid-driven cavity, flow through a gradual expansion and laminar flow in a three-dimensional curved duct of square cross section. The cases were selected because they have been extensively studied in the literature and benchmark solutions are available.

All predictions were made with E-factors and pressure relaxation values of approximately 3 and 0·8 respectively. Solutions were assumed to be converged when the average, steady state, momentum residuals had decreased by five orders of magnitude over the initial residual values. Mass residuals were not used to monitor convergence, because the projection method in conjunction with the algebraic multigrid solver drove the mass imbalances to near round-off for each global iteration or time step. For all cases, grid-independent solutions were obtained.

3.1. *Lid-driven cavity flow*

The first test case involves laminar flow in a square cavity which is driven by a moving lid. This is a standard problem to test the accuracy and convergence characteristics of fluid flow algorithms.[16,40,41] The geometry is square ($L_y/L_x = 1$). At the bottom, left and right boundaries the velocity is constrained to zero, while a uniform horizontal velocity is imposed at the top boundary. The present case was based on a Reynolds number of 400.

A number of grids and differencing schemes were considered. The grids included 20 × 20, 40 × 40 and 80 × 80 uniform discretizations. The differencing schemes included MINMOD, OSHER, MUSCL, CLAM, SMART and UPWIND. Predictions from the current algorithms were compared with predictions of Ghia *et al.*[41] and predictions from a cell-centred, finite volume code with a hybrid differencing scheme (FVM-CC). The Ghia *et al.* results are from a 129 × 129 uniform grid. All comparisons were made using the normalized horizontal velocity at the vertical centreline.

Figure 5 compares results for the SMART scheme for a number of different grids. As the grid is refined, the present predictions approach those of Ghia *et al.*[41] Results for the 40 × 40 and 80 × 80 grids are nearly identical, indicating that the 80 × 80 solution is essentially grid-independent. Figures 6(a) and 6(b) contrast the various differencing schemes for the 40 × 40 discretization. As seen in Figure 6(a), all the high-resolution schemes yield accurate solutions, with no scheme performing better or worse than another. In contrast, Figure 6(b) displays the diffusive nature of the upwind and hybrid schemes. As expected, the upwind scheme is the most diffusive, while the hybrid scheme lies between the upwind and high-resolution schemes. The predictions of the HR schemes (MINMOD, MUSCL, OSHER, CLAM and SMART) compare very favourably with predictions of other workers. The solutions for the 40 × 40 grid are very close to the grid-independent solutions obtained by Ghia *et al.* using a vorticity–streamfunction approach.

The global convergence rates for the 40 × 40 grid are shown in Figure 7. All HR schemes have very similar convergence histories. The UPWIND scheme converges slightly better than the high-resolution schemes; however, the increased accuracy of the HR schemes more than offsets the slight increase in computational costs. For the cavity case the differences between convergence histories are solely due to the advection differencing scheme and deferred correction procedure, because the grid is orthogonal and thus all discrete Laplacian operators are treated implicitly.

3.2. *Flow through a gradual expansion*

Flow through a gradual expansion was considered. This benchmark case was developed by Roache[42] and was later adopted at the Fifth Meeting of the International Association for Hydraulic Research (IAHR) Working Group on Refined Modelling of Flows.[43] The geometry for the problem is shown in Figure 8 and is dependent on the Reynolds number. Two Reynolds numbers, 10 and 100, are considered. The axial inlet velocity profile is parabolic, while the inlet transverse velocity is zero.

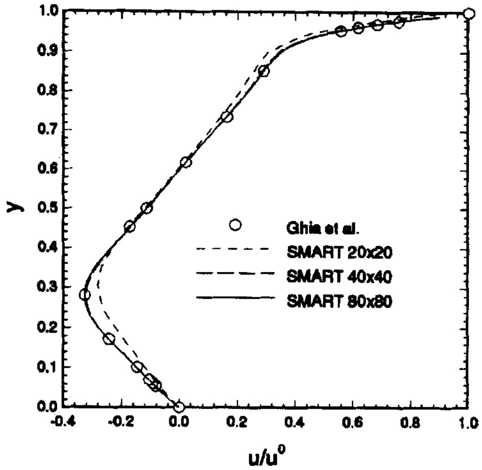

Figure 5. Sensitivity of solutions to grid refinement for driven cavity case

For both Reynolds number flows, grid dependence was investigated by performing calculations on successively finer grids: 20 × 10, 40 × 20 and 80 × 40. The 40 × 20 grid for the $Re = 10$ case is shown in Figure 1. Grid sensitivity is investigated in Figure 9 for a Reynolds number of 100. Variations are evident in the 20 × 10 grid solutions near the inlet, but the solutions of the 40 × 20 and 80 × 40 grids are nearly coincident, with a maximum difference of 1·6%. Excellent agreement is shown with the benchmark solution of Cliffe *et al.* as reported by Napolitano and Orlandi.[43]

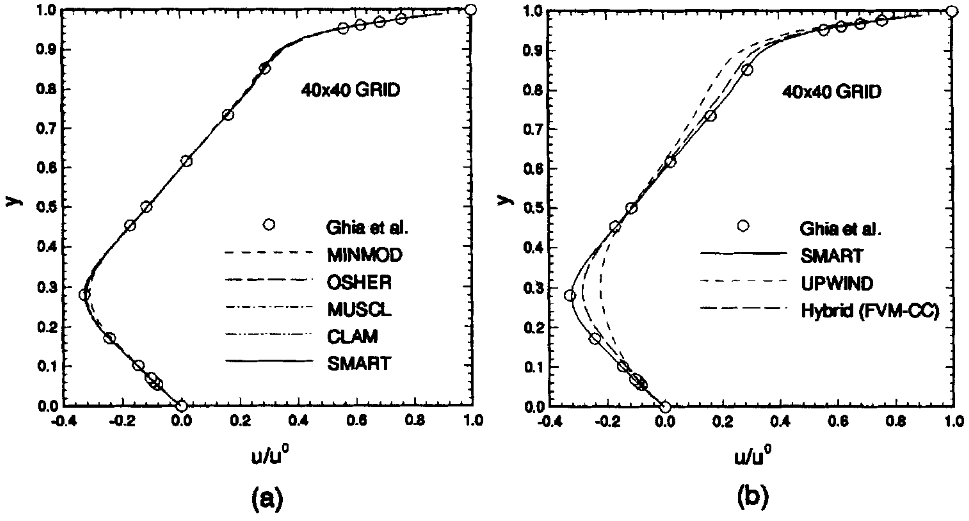

(a) (b)

Figure 6. Comparison of horizontal velocity for driven cavity case ($x = 0{\cdot}5$)

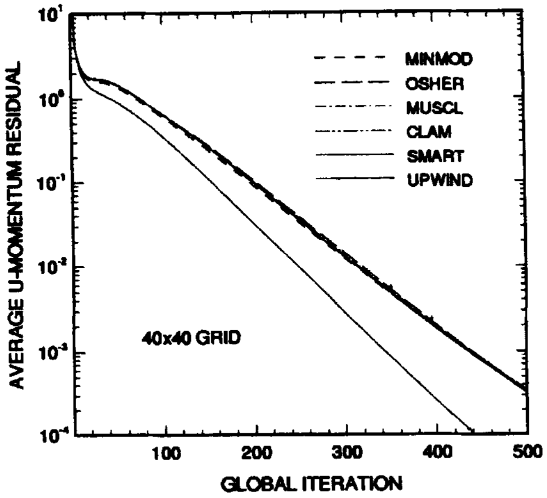

Figure 7. Residuals for driven cavity case

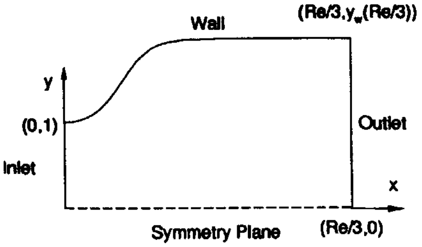

Figure 8. Geometry for gradual expansion case

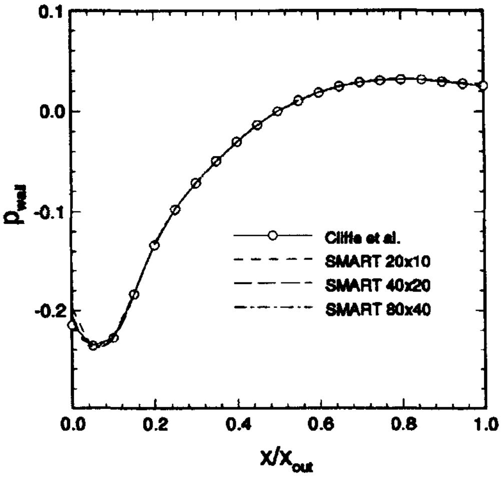

Figure 9. Sensitivity of predicted wall pressure to grid refinment for gradual expansion case

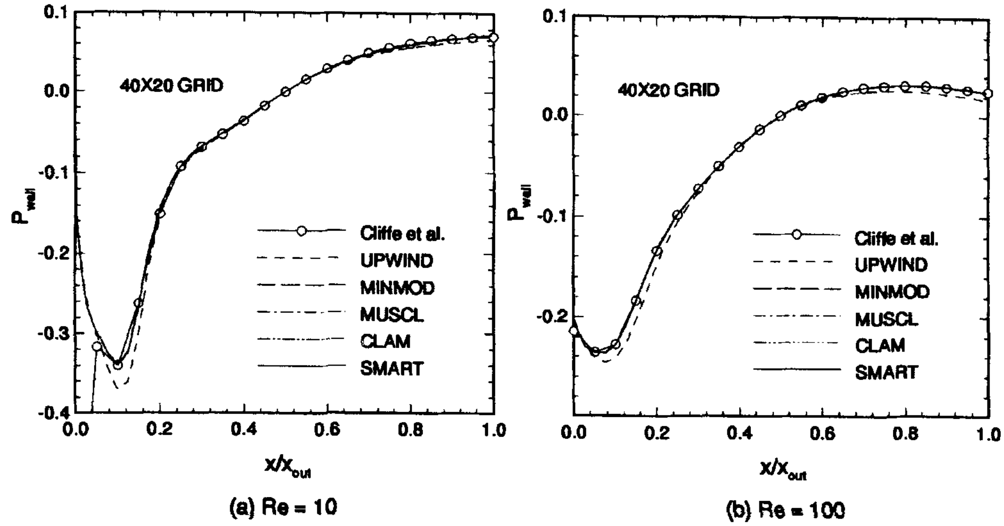

Figure 10. Comparison of predicted wall pressure for gradual expansion case

The sensitivity of the solutions to the differencing scheme is displayed in Figure 10. Results are shown for the upwind and four HR schemes. For both Reynolds numbers the predictions from the HR schemes are similar and very close to the benchmark solutions, while the upwind predictions are less accurate. The relative accuracy of the solutions is quantified by the error norm

$$\varepsilon_p = \frac{100}{19} \sum_{i=2}^{20} \left| \frac{p_i - p_{\mathrm{CJG},i}}{p_{\mathrm{CJG},i}} \right|, \tag{44}$$

where p_i is the predicted pressure at a number of evenly spaced points on the wall and $p_{\mathrm{CJG},i}$ is the assumed grid-independent solution of Cliffe *et al.* The results are compared with those of other workers in Table I. The present predictions show excellent agreement with the benchmark of Cliffe *et al.*

Table I. Comparison of error for gradual expansion case ($Re = 100$)

Investigator(s)	Method[b]	$\varepsilon_p(\%)$[c]
Present[a]	FV	0·69
Alfrink	FV	10·02
Demirdzic and Gosman	FV	6·77
Grandotto	FE	1·43
Goussebaile *et al.*	FD	17·61
Guj and Faviani	FD	2·71
Hutton	FE	1·50
Latrobe and Delapierre	FV	12·31
Magi and Napolitano	FD	33·45
Porter *et al.*	FD	7·15

[a] SMART scheme, 40 × 20 grid.
[b] FD, finite difference; FE, finite element; FV, finite volume.
[c] Data reported by Napolitano and Orlandi.[43]

3.3. *Laminar flow in a curved duct*

Three-dimensional laminar flow in a curved duct of square cross-section[44] was considered. The case is a standard benchmark case for three-dimensional internal flows.[40,44,45] The geometry and actual operating conditions are documented by Humphrey *et al.*[44] The Reynolds number based on the hydraulic diameter and bulk velocity is 790.

The physical domain was represented individually by a number of computational grids: 20 × 10 × 60, 28 × 14 × 84 and 40 × 20 × 120. The coarsest grid (20 × 10 × 60) is shown in Figure 11. Owing to symmetry, only one half of the physical domain was modelled. The computational domain started at five hydraulic diameters upstream of the bend and continued for five hydraulic diameters downstream of the bend. A fully developed velocity profile was assumed at the inlet of the domain.

The predictions are compared with experimental data[44] in Figure 12. Comparisons are made at five longitudinal locations: $x = -2{\cdot}5D_\mathrm{h}$, $\theta = 0°$, $\theta = 30°$, $\theta = 60°$ and $\theta = 90\,\mathrm{deg}$. At each location the velocity profiles are plotted along two lines: $z/D_\mathrm{h} = 0$ (centreline) and $z/D_\mathrm{h} = 0{\cdot}25$. The strong curvature of the duct generates a strong secondary flow, due to centrifugal forces and adverse and favourable longitudinal pressure gradients at the inner and outer radii respectively. The predictions compare well with the data at all locations. Similar results were obtained by Choi *et al.*,[10] Rosenfeld *et al.*[45] and Rogers *et al.*[46] The sensitivity of the predictions to the differencing scheme is shown in Figure 13 for the 28 × 14 × 84 grid at one location. The SMART scheme performs best. The MINMOD scheme is slightly less accurate, but this may be expected since the MINMOD scheme is second-order in the monotonic range while the SMART scheme is third-order. The first-order upwind scheme again exhibits large amounts of numerical diffusion. The convergence histories for the three considered schemes are shown in Figure 14. The convergence rate is good for all schemes, with that of the upwind being better than those of the two HR schemes.

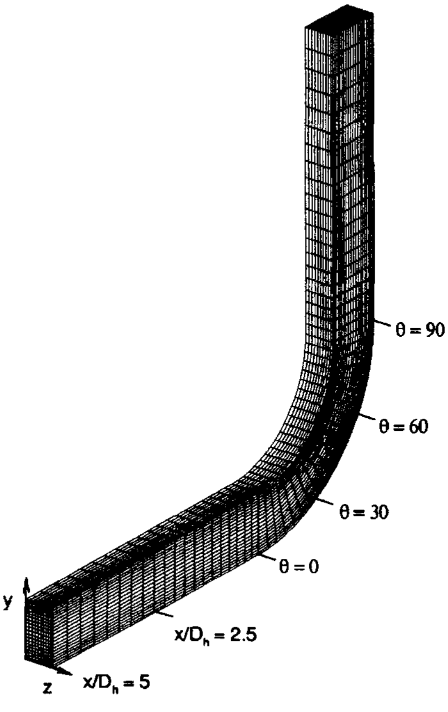

Figure 11. Computational grid for curved duct case (20 × 10 × 60)

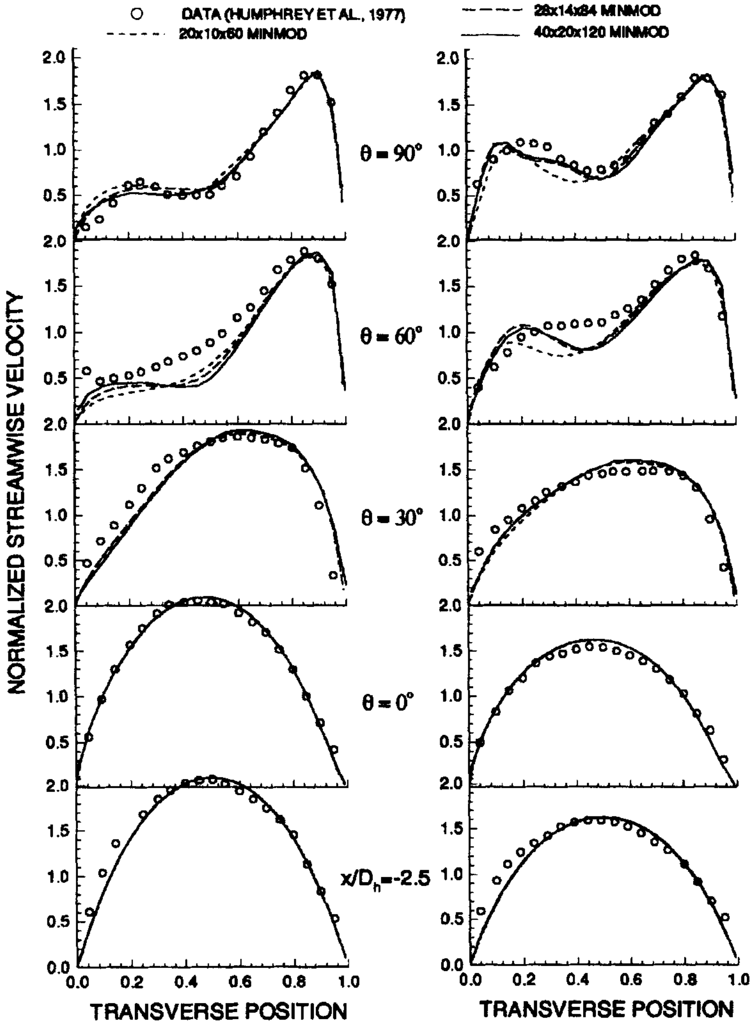

(a) $z/D_h = 0$ (b) $z/D_h = 0.25$

Figure 12. Comparison of predicted and measured streamwise velocity for curved duct case

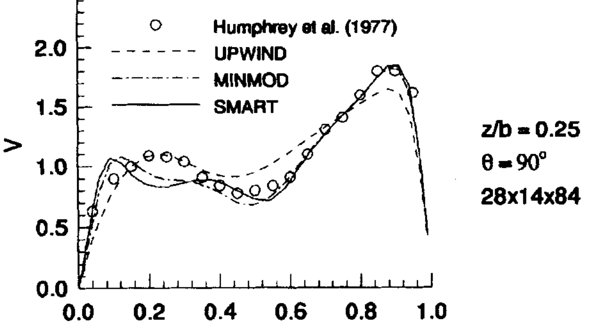

Figure 13. Comparison of differencing schemes for curved duct case

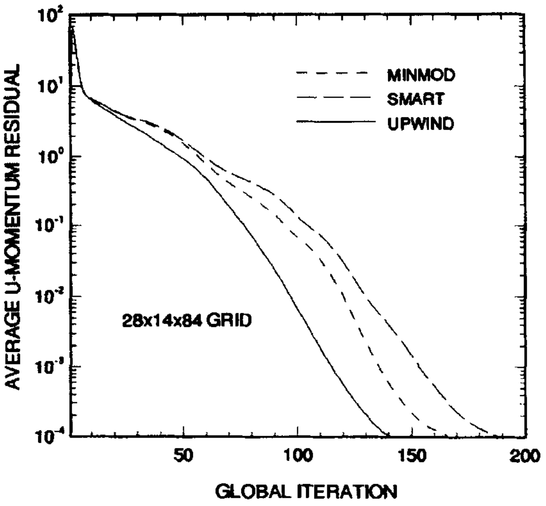

Figure 14. Residuals for curved duct case

4. CONCLUSIONS

A non-orthogonal, finite volume algorithm for the solution of the incompressible Navier–Stokes equations has been presented. High-resolution differencing schemes were incorporated to provide bounded solutions with low numerical diffusion. A form of Rhie and Chow interpolation was employed to ensure coupling of the pressure and velocity fields. The mass and momentum equations were solved using a projection method to guarantee conservation of mass during each step of the algorithm. The inclusion of the non-orthogonal terms in the discrete pressure Poisson equation was found to be crucial with highly non-orthogonal grids.

A number of standard benchmark cases were investigated. Grid-independent solutions were obtained for all cases. The high-resolution schemes produced much more accurate solutions than the first-order schemes. The cavity and gradual expansion cases indicated no clear preference among the high-resolution schemes themselves with regard to accuracy; however, for the curved duct case the third-order SMART scheme produced a more accurate solution than the second-order MINMOD scheme. The high-resolution schemes in conjunction with the deferred correction procedure slightly degraded the global convergence of the steady state equations compared with the upwind scheme. Nevertheless, the increased computation time is quite insignificant compared with the increased accuracy of the high-resolution schemes. Alternative time discretization and linearization methods may improve the convergence rates.

Although all test cases employed structured grids, the present algorithm is applicable to unstructured meshes of quadrilateral and hexahedral elements. Future work will focus on implementing turbulence and chemical reaction models and adding triangular and tetrahedral element capabilities.

APPENDIX: NOMENCLATURE

a	coefficient of discrete transport equation
ΔA	area
b	constant term in discrete transport equation
C, D, U	nodal indices for advection stencil
D	pressure gradient coefficient in discrete momenum equation

E	E-factor
$F^{\mathrm{I}}, G^{\mathrm{I}}$	inviscid fluxes
$F^{\mathrm{V}}, G^{\mathrm{V}}$	viscous fluxes
H	portion of discrete momenum equation
i, j	unit vectors in x- and y-direction, respectively
I, J	nodal indices
n	unit normal vector
p	pressure
Q	dependent variable vector
Re	Reynolds number
S	source term
t	time (s)
u	vector velocity (m s^{-1})
u	face x-direction velocity (m s^{-1})
U	x-direction velocity (m s^{-1})
v	face y-direction velocity (m s^{-1})
V	y-direction velocity (m s^{-1})
ΔV	volume (m^3)
x	spatial co-ordinmate (m)
y	spatial co-ordinate (m)

Greek letters

α	relaxation factor
β	coefficient in discrete momentum equation
γ	term in discrete momentum equation
Γ	diffusion coefficient; spatial domain boundary
Δ	difference operator
ε	error
Λ	spatial domain
ξ	local parametric co-ordinate
τ	stress tensor
ρ	density (kg m^{-3})
ϕ	general transport variable

Subscripts

f	face value
I, J	nodal indices
j	face or control surface index
p	pressure
x	x-direction
y	y-direction

Superscripts

0	previous iterate or time step
a	advection
c	continuity equation

d	diffusion
n	time step or iterate index
p	pressure
p'	pressure correction equation
s	source
t	transient
u, v	face velocities
U	x-direction momentum equation
V	y-direction momentum equation
ϕ	general transport equation
$'$	correction
$*$	intermediate value

Special symbols

∇	nabla, gradient vector
$\vec{}$	vector
$\hat{}$	unit vector
$\tilde{}$	normalized quantity

REFERENCES

1. T. J. Barth, 'Numerical aspects of computing viscous high Reynolds number flows on unstructured meshes', *AIAA Paper 91-0721*, 1991.
2. D. Pan and J.-C. Cheng, 'Upwind finite volume Navier–Stokes computations on unstructured triangular meshes', *AIAA J.*, **31**, 1618–1625 (1993).
3. J. K. Watterson, 'A pressure-based flow solver for the three-dimensional Navier–Stokes equations on unstructured and adaptive meshes', *AIAA Paper 94-2358*, 1994.
4. B. P. Leonard, 'A stable and accurate convective modelling procedure based on quadratic interpolation', *Comput. Methods Appl. Mech. Eng.*, **19**, 59–98 (1979).
5. M. S. Darwish, 'A new high resolution scheme based on the normalized variable formulation', *Numer. Heat Transfer B*, **24**, 287–307 (1993).
6. F. H. Harlow and J. E. Welch, 'Numerical calculation of time-dependent viscous incompressible flow of fluid with free surface', *Phys. Fluids*, **8**, 2182–2189 (1965).
7. C. M. Rhie and W. L. Chow, 'Numerical study of the turbulent flow past an airfoil with trailing edge separation', *AIAA J.*, **21**, 1525–1532 (1983).
8. K. H. Chen and R. H. Pletcher, 'Primitive variable, strongly implicit calculation procedure for viscous flows at all speeds', *AIAA J.*, **29**, 1241–1249 (1991).
9. D. Kwak and S. R. Chakravarthy, 'A three-dimensional incompressible Navier–Stokes flow solver using primitive variables', *AIAA J.*, **24**, 390–396 (1986).
10. S. K. Choi, H. Y. Nam, Y. B. Lee and M. Cho, 'An efficient three-dimensional calculation procedure for incompressible flows in complex geometries', *Numer. Heat Transfer B*, **23**, 387–400 (1993).
11. M. Majumdar, 'Role of underrelaxation in momentum interpolation for calculation of flow with nonstaggered grids', *Numer. Heat Transfer*, **13**, 125–132 (1988).
12. M. Peric, R. Kessler and G. Scheurer, 'Comparison of finite volume numerical methods with staggered and colocated grids', *Comput. Fluids*, **16**, 389–403 (1988).
13. T. F. Miller and F. W. Schmidt, 'Use of a pressure-weighted interpolation method for solution of the incompressible Navier–Stokes equations on a nonstaggered grid system', *Numer. Heat Transfer*, **14**, 213–233 (1988).
14. M. H. Kobayshi and J. C. F. Pereira, 'Numerical comparisons of momentum interpolation methods and pressure–velocity algorithm using nonstaggered grids', *Commun. Appl. Numer. Methods*, **7**, 173–186 (1991).
15. S. P. Vanka, 'Block-implicit multigrid solution of Navier-Stokes equations in primitive variables', *J. Comput. Phys.*, **65**, 138–158 (1986).
16. M. Williams, 'Methods for calculating incompressible viscous flows', *Numer. Heat Transfer B*, **20**, 241–253 (1991).
17. B. R. Baliga and S. V. Patankar, 'A new finite-element formulation for convection–diffusion problems', *Numer. Heat Transfer*, **3**, 393–409 (1980).

18. G. E. Schneider and M. J. Raw, 'Control-volume finite-element method for heat transfer and fluid flow using collocated variables—1. Computational procedure', *Numer. Heat Transfer*, **11**, 363–390 (1987).
19. C. A. J. Fletcher, *Computational Techniques for Fluid Dynamics*, Vol. II, 2nd edn, Springer, Berlin, 1991.
20. C. Prakash and S. V. Patankar, 'A control-volume-based finite-element method for solving the Navier–Stokes equations using equal-order velocity–pressure interpolation', *Numer. Heat Transfer*, **8**, 259–280 (1985).
21. O. C. Zienkiewicz and R. L. Taylor, *The Finite Element Method*, Vol. 1, 4th edn, McGraw-Hill, New York, 1989.
22. T. J. Barth and D. C. Jespersen, 'The design and application of upwind schemes on unstructured meshes', *AIAA Paper 89-0366*, 1989.
23. G. E. Schneider, 'Elliptic systems: finite-element method I', in W. J. Minkowycz, E. M. Sparrow, G. E. Schneider and R. H. Pletcher (eds), *Handbook of Numerical Heat Transfer*, Wiley, New York, 1988, Chap. 10, pp. 379–420.
24. M. S. Darwish and F. H. Moukalled, 'Normalized variable and space formulation methodology for high resolution schemes', *Numer. Heat Transfer B*, **26**, 79–96 (1994).
25. P. R. M. Lyra, K. Morgan, J. Peraire and J. Peiro, 'Unstructured grid FEM/TVD algorithm for systems of hyperbolic conservation laws', *Proc. 8th Int. Conf. on Numerical Methods in Laminar and Turbulent Flow*, Pineridge, Swansea, 1993, pp. 1408–1420.
26. J. Cabello and K. Morgan, 'A comparison of higher order schemes used in a finite volume solver for unstructured grids', *AIAA Paper 94-2293*, 1994.
27. B. P. Leonard, 'A survey of finite differences with upwinding for numerical modelling of the incompressible convection diffusion equations', in C. Taylor and K. Morgan (eds), *Computational Techniques in Transient and Turbulent Flow*, Vol. 2, Pineridge, Swansea, 1981, pp. 1–35.
28. A. Harten, 'High resolution schemes for hyperbolic conservation laws', *J. Comput. Phys.*, **49**, 357–393 (1983).
29. S. R. Chakravarthy and S. Osher, 'High resolution application of the OSHER upwind scheme for the Euler equations', *AIAA Paper 83-1943*, 1983.
30. B. Van Leer, 'Towards the ultimate conservation difference scheme. V. A second-order sequel to Godunov's method', *J. Comput. Phys.*, **23**, 101–136 (1977).
31. B. Van Leer, 'Towards the ultimate conservation difference scheme. II. Monotonicity and conservation combined in a second-order scheme', *J. Comput. Phys.*, **14**, 361–370 (1974).
32. P. H. Gaskell and A. K. C. Lau, 'Curvature compensated convective transport: SMART, a new boundedness preserving transport algorithm', *Int. j. numer. methods fluids*, **8**, 617–641 (1988).
33. J. Zhu and W. Rodi, 'A low dispersion and bounded convection scheme', *Comput. Methods Appl. Mech. Eng.*, **92**, 87–96 (1991).
34. S. V. Patankar and D. B. Spalding, 'A calculation procedure for heat, mass and momentum transfer in three-dimensional parabolic flows', *Int. J. Heat Mass Transfer*, **15**, 1787–1806 (1972).
35. A. J. Chorin 'A numerical method for solving incompressible viscous flow problems', *J. Comput. Phys.*, **2**, 12–26 (1967).
36. C. Hirsch, *Numerical Computation of Internal and External Flows*, Wiley, New York, 1990.
37. J. P. Van Doormaal and G. D. Raithby, 'Enhancements of the SIMPLE method for predicting incompressible fluid flows', *Numer. Heat Transfer*, **7**, 147–163 (1984).
38. B. R. Hutchinson and G. D. Raithby, 'A multigrid method based on the additive correction strategy', *Numer. Heat Transfer*, **9**, 511–537 (1986).
39. J. W. Ruge and K. Stüben, 'Algebraic multigrid', in S. McCormick (ed.), *SIAM Frontier Series*, Vol. 3, pp. 73–130, *Multigrid Methods*, SIAM Philadelphia, PA, 1987.
40. O. R. Burggraf, 'Analytical and numerical studies of the structure of steady separated flows', *J. Fluid Mech.*, **24**, 113 (1966).
41. U. Ghia, K. N. Ghia and C. T. Shin, 'High-resolutions for incompressible flow using the Navier–Stokes equations and a multigrid method', *J. Comput. Phys.*, **48**, 387–411 (1982).
42. P. Roache, 'Scaling of high Reynolds number weakly separated channel flows', *Proc. Symp. on Numerical and Physical Aspects of Aerodynamic Flows*, pp. 87–98, 1981.
43. M. Napolitano and P. Orlandi, 'Laminar flow in a complex geometry: a comparison', *Int. j. numer. methods fluids*, **5**, 667–683 (1985).
44. J. A. Humphrey, A. M. K. Taylor and J. H. Whitelaw, 'Laminar flow in a square duct of strong curvature', *J. Fluid Mech.*, **83**, 509–527 (1977).
45. M. Rosenfeld, D. Kwak and M. Vinokur, 'A fractional step solution method for the unsteady incompressible Navier–Stokes equation in generalized coordinate system', *J. Comput. Phys.*, **94**, 102–137 (1991).
46. S. E. Rogers, D. Kwak and C. Kiris, 'Steady and unsteady solutions of the incompressible Navier–Stokes equations', *AIAA J.*, **29**, 603–610 (1991).